International Journal of Biological Macromolecules 120 (2018) 835–845

Contents lists available at ScienceDirect

International Journal of Biological Macromolecules

journal homepage: http://www.elsevier.com/locate/ijbiomac

Unique N-terminal extension domain of human asparaginyl-tRNA synthetase elicits CCR3-mediated chemokine activity

Joon Sung Park [a], Min Chul Park [b], Ki-Young Lee [a], Peter C. Goughnour [b], Seung Jae Jeong [b], Hyoun Sook Kim [c], Hyun-Jung Kim [d], Bong-Jin Lee [a], Sunghoon Kim [b], Byung Woo Han [a,*]

[a] Research Institute of Pharmaceutical Sciences, College of Pharmacy, Seoul National University, Seoul 08826, Republic of Korea
[b] Medicinal Bioconvergence Research Center, Seoul National University, Seoul 08826, Republic of Korea
[c] Therapeutic Target Discovery Branch, Division of Precision Medicine and Cancer Informatics, Research Institute, National Cancer Center, Goyang-si, Gyeonggi-do 10408, Republic of Korea
[d] College of Pharmacy, Chung-Ang University, Seoul 06974, Republic of Korea

ARTICLE INFO

Article history:
Received 4 April 2018
Received in revised form 24 August 2018
Accepted 28 August 2018
Available online 30 August 2018

Keywords:
Asparaginyl-tRNA synthetase
Chemokine
C—C chemokine receptor 3

ABSTRACT

Asparaginyl-tRNA synthetase (NRS) is not only essential in protein translation but also associated with autoimmune diseases. Particularly, patients with antibodies that recognize NRS often develop interstitial lung disease (ILD). However, the underlying mechanism of how NRS is recognized by immune cells and provokes inflammatory responses is not well-understood. Here, we found that the crystal structure of the unique N-terminal extension domain of human NRS (named as UNE-N, where -N denotes NRS) resembles that of the chemotactic N-terminal domain of NRS from a filarial nematode, *Brugia malayi*, which recruits and activates specific immune cells by interacting with CXC chemokine receptor 1 and 2. UNE-N induced migration of C—C chemokine receptor 3 (CCR3)-expressing cells. The chemokine activity of UNE-N was significantly reduced by suppressing CCR3 expression with CCR3-targeting siRNA, and the loop3 region of UNE-N was shown to interact mainly with the extracellular domains of CCR3 in nuclear magnetic resonance perturbation experiments. Based on these results, evolutionarily acquired UNE-N elicits chemokine activities that would promote NRS-CCR3-mediated proinflammatory signaling in ILD.

1. Introduction

Aminoacyl-tRNA synthetases (ARSs) play a fundamental role in protein synthesis by charging tRNA with its respective amino acid. Interestingly, autoantibodies against at least eight ARSs have been identified in antisynthetase syndrome associated with interstitial lung disease (ILD) and idiopathic inflammatory myopathies [1–3]. Autoantibody-targeted ARSs are released under specific immune conditions and some are known to elicit chemotactic activity [4–6]. Anti-Jo-1, autoantibodies to histidyl-tRNA synthetase, is most frequently observed in antisynthetase syndrome, and histidyl-tRNA synthetase has been shown to induce migration of $CD4^+$ and $CD8^+$ lymphocytes, interleukin-2-activated monocytes, and immature dendritic cells (iDCs) in a CC-chemokine receptor (CCR) 5-dependent manner. Anti-KS, autoantibodies to asparaginyl-tRNA synthetase (NRS), is often detected in patients with ILD, but is much lower in those with myositis, and NRS recruits iDCs in a CCR3-dependent manner [4]. However, it remains unclear how these protein synthesis enzymes interact with receptors on immune cells and elicit non-translational functions.

In addition to their translational functions, higher eukaryotic ARSs are known to play roles in various physiological events such as vascular development, angiogenesis, cytokine signaling, tumorigenesis, inflammation, apoptosis, neural development, and immunological response via its evolutionarily acquired domains and alternative splicing variants with catalytic nulls [7–10]. Higher eukaryotes have also developed a multi-aminoacyl-tRNA synthetase complex that serves as a reservoir for nine ARSs and as regulatory machinery of non-translational functions of the component proteins [7,11,12].

NRS is a class 2b ARS along with aspartyl-tRNA synthetase and lysyl-tRNA synthetase and contains a unique N-terminal extension domain (named as UNE-N, where -N denotes NRS). Eukaryotic class 2b ARSs share common sequence motifs in their canonical domain for their translational function but contain N-terminal extension domains that serve additional non-translational functions [13–19]. For example, the UNE-N domain from a filarial nematode, *Brugia malayi*, participates in

Abbreviations: NRS, (human) asparaginyl-tRNA synthetase; UNE-N, unique N-terminal extension domain of NRS; CD, canonical domain; *Bm*NRS, *Brugia malayi* NRS; CCR3, C—C chemokine receptor 3; ILD, interstitial lung disease; SAD, single-wavelength anomalous diffraction; RMSD, root-mean-square deviation.

* Corresponding author.
E-mail address: bwhan@snu.ac.kr (B.W. Han).

https://doi.org/10.1016/j.ijbiomac.2018.08.171
0141-8130/

the development of pathological responses through interleukin 8-like activity that targets CXC-chemokine receptor 1 (CXCR1) and 2 (CXCR2), thus modulating the host immune system [20–23].

Human NRS is also clearly connected to immunological disorders and plays a role in modulating receptors on immune cells. To determine the relationships between NRS, CCR3, and autoimmune diseases at a molecular level, we determined the crystal structures of UNE-N and canonical domain (CD) of human NRS and further examined the molecular dynamics of UNE-N as an effector domain for recruiting CCR3. We then investigated the conditions under which NRS is secreted and chemokine activity induces migration of immune cells. To validate the direct interaction between NRS and CCR3, we conducted pull-down assays and examined nuclear magnetic resonance (NMR) chemical shift/perturbation changes in UNE-N in the absence and presence of each extracellular domain (ED) of CCR3. Based on our results, we suggest that the evolutionarily acquired UNE-N plays an important role in CCR3-mediated proinflammatory signaling in ILD and the interaction between UNE-N and CCR3 requires further analysis to determine how it controls CCR3-related diseases.

2. Materials and methods

2.1. Cloning, protein expression, and purification

NRS constructs for CD (residues 98–548) and UNE-N variants (residues 1–77, 4–77, and 1–111) were designed based on secondary structure prediction with the XtalPred server [24] and structures of *Bm*NRS [18].

NRS and CD (residues 98–548) were cloned into pET-28a(+) between the Nde1 and Xho1 restriction sites. Each construct contained an N-terminal hexahistidine tag. NRS and CD were overexpressed in the C41 (DE3) and Solu-BL21, *Escherichia coli* (*E. coli*) strains, respectively. The transformed cells were grown at 37 °C to an OD_{600} of 0.5 in Luria-Bertani media containing kanamycin and protein expression was induced by 0.5 mM isopropyl β-D-1-thiogalactopyranoside. The cells were incubated for additional 8 h and then harvested by centrifugation at 6000 ×*g* for 10 min. The harvested cells were resuspended in buffer A (500 mM NaCl, 20 mM Tris-HCl, 35 mM imidazole, pH 7.5) with 1 mM phenylmethylsulfonyl fluoride and lysed by sonication. Lysed cells were centrifuged at 35,000 ×*g* for 1 h. The resulting supernatants were filtered with a 0.45-μm syringe filter device (Sartorius, Göttingen, Germany) and loaded onto a 5-mL HiTrap chelating HP column (GE Healthcare, Little Chalfont, UK) which had been pre-charged with Ni^{2+} and equilibrated with buffer A. After washing with buffer A, the retained proteins were eluted by addition of an increasing gradient of buffer B (500 mM NaCl, 20 mM Tris-HCl, 1 M imidazole, pH 7.5). The proteins were loaded onto a HiPrep desalting 26/10 column (GE Healthcare) and eluted with buffer C (50 mM NaCl, 20 mM Tris-HCl, pH 7.5). The eluates were loaded onto a HiTrap 5-mL Q HP (GE Healthcare) column. The loaded column was washed with buffer C and the retained proteins were eluted with a gradient of buffer D (1 M NaCl, 20 mM Tris-HCl, pH 7.5). The proteins were finally purified over a HiLoad 16/600 Superdex 200 pg (GE Healthcare) column with appropriate buffers: buffer E (200 mM NaCl, 10 mM Tris-HCl, pH 7.5) for crystallization and phosphate-buffered saline (PBS, 137 mM NaCl, 2.7 mM KCl, 4.3 mM Na_2HPO_4, 1.4 mM KH_2PO_4, pH 7.4) for the cell migration assay.

The UNE-N constructs were PCR-amplified and cloned into pET-28a (+) (Novagen, Madison, WI, USA) with Nde1 and Xho1 restriction sites. Each construct contained a hexahistidine tag, MBP, and tobacco etch virus (TEV) protease cleavage site at the N-terminus. Recombinant proteins were overexpressed in Rosetta 2(DE3), an *E. coli* strain. *E. coli* growth, protein expression, and purification up to hexahistidine tag affinity chromatography were same as the procedure used for NRS purification. The proteins purified by affinity chromatography were loaded onto a HiPrep desalting 26/10 column (GE Healthcare) and eluted with buffer E. The eluates were incubated with TEV protease at 4 °C overnight to cleave the MBP tag. The proteins were loaded onto a HiTrap 5-mL chelating HP column (GE Healthcare) pre-charged with Ni^{2+} and equilibrated with buffer E. The proteins in the flow-through fractions were loaded onto a HiLoad 16/600 Superdex 75 pg column (GE Healthcare) and eluted with appropriate buffers: buffer F (200 mM NaCl, 10 mM Tris-HCl, pH 8.5) for crystallization; PBS for cell migration assay; buffer G (150 mM NaCl, 20 mM NaH_2PO_4/Na_2HPO_4, pH 6.5), and buffer H (150 mM NaCl, 20 mM NaH_2PO_4/Na_2HPO_4, pH 7.5) for NMR experiments.

The four CCR3 ED sequences are as follows: ED1 (residues 1–40, MTTSLDTVET FGTTSYYDDV GLLCEKADTR ALMAQFVPPL), ED2 (residues 94–120, VRGHNWVFGH GMCKLLSGFY HTGLYSE), ED3 (residues 172–203, YETEELFEET LCSALYPEDT VYSWRHFHTL RM), and ED4 (residues 262–281, SSYQSILFGN DCERSKHLDL). MBP-fused CCR3 EDs were PCR-amplified and cloned into pET-28a(+) (Novagen) with Nde1 and Xho1 restriction sites. Each construct contained hexahistidine tag at the N-terminus and TEV protease cleavage site between MBP and CCR3 EDs. Recombinant proteins were overexpressed in Rosetta 2 (DE3), an *E. coli* strain. *E. coli* growth, protein expression, and purification steps up to hexahistidine tag affinity chromatography were same as those used for NRS purification. The proteins purified by affinity chromatography were loaded onto a HiLoad 16/600 Superdex 200 pg column (GE Healthcare) and eluted with appropriate buffers: PBS for the pull-down assay and buffer H for NMR experiments.

2.2. Selenomethionine incorporation

For the selenomethionine-derived protein, UNE-N was overexpressed in B834(DE3), an *E. coli* strain. The cells were cultured in media containing M9, minimal salts (Sigma-Aldrich, St. Louis, MO, USA), and amino acid mix containing L-selenomethionine. Protein expression and purification were conducted in the same manner as UNE-N purification.

2.3. Crystallography

Purified UNE-N and CD proteins were crystallized at 22 °C using the sitting drop vapor diffusion method with 1 μL protein and 1 μL crystallization solution. Initial crystals of UNE-N (residues 4–77) were grown under commercial crystallization screening conditions with 0.01 M zinc sulfate, 0.1 M MES (pH 6.5), and 25% (*v*/v) polyethylene glycol (PEG) 550 monomethyl ether (Structure Screen 2, Molecular Dimensions, Suffolk, UK). Initial crystals were further optimized for diffraction data collection. The crystal was cryoprotected with reservoir solution supplemented with 12.5% of glycerol and flash-frozen in a nitrogen gas stream at 100 K. Single-wavelength anomalous diffraction data were collected at the synchrotron beamline 5C of the Pohang Light Source, Republic of Korea, at an anomalous peak wavelength (0.9796 Å). Collected data were processed at 1.9 Å resolution using the *HKL2000* program suite [25]. The phase problem was solved by the single anomalous diffraction (SAD) method and an initial model was built using the AutoSol program of the PHENIX software package [26] and improved by density modification using the automatic model building program Resolve [27]. For the final model, another diffraction data set was collected from a selenomethionine-derived protein crystal and processed at 1.65 Å resolution. The initial model from the SAD method was used as a template for molecular replacement using the Phaser program [28].

Initial crystals of CD were grown from a commercial crystallization screening condition with 20% (v/v) glycerol, 0.04 M potassium phosphate, and 16% (w/v) PEG 8000 (Wizard Classic 4, Rigaku, Tokyo, Japan). Initial crystals were further optimized for diffraction data collection. The crystal was flash-frozen in a nitrogen gas stream at 100 K. Diffraction data were collected at the synchrotron beamline AR-NW12A of the Photon Factory, Japan, and processed at 2.25 Å resolution using the HKL2000 program suite [25]. The structure was solved by molecular replacement using the MOLREP program [29] with the crystal structure of *Bm*NRS (PDB ID: 2XGT) [18] as a phasing model.

Model building, refinement, and validation for crystal structures were carried out with the WinCoot program [30], phenix.refine [31],

and MOLPROBITY [32], respectively. Data collection and refinement statistics are summarized in Table 1. The secondary structure of our crystal structures were analyzed in DSSP program analysis [33,34].

2.4. NMR analysis of UNE-N

Uniformly ^{15}N- and ^{13}C-labeled or ^{15}N-labeled UNE-N were prepared by growing the cells in M9 medium, which contained 99% $^{15}NH_4Cl$ and 99% [^{13}C]-D-glucose (Cambridge Isotope Laboratories, Tewksbury, MA, USA). The proteins for three-dimensional (3D), hetero-nuclear NOE, and CLEANEX-PM NMR experiments were prepared at a concentration of approximately 0.6 mM in buffer G with 10% D_2O. For NMR titration experiments with CCR3 EDs, ^{15}N-labeled UNE-N and unlabeled CCR3 EDs were prepared at concentrations of approximately 0.2–0.3 and 0.2–0.6 mM, respectively, in buffer F with 10% D_2O. The NMR experiments were carried out at 298 K on a Bruker AVANCE 800 spectrometer (Billerica, MA, USA) equipped with a cryogenic probe and on Jeol ECA 600 spectrometer (Tokyo, Japan). Backbone peak assignments of UNE-N were performed using a series of triple resonance spectra [3D HNCO, HN(CA)CO, HNCACB, CBCA(CO)NH]. NMR data were processed with the program NMRPipe [35] and analyzed with the program NMRViewJ (http://www.onemoonscientific.com/nmrviewj). The overall secondary structure was derived from chemical shifts using the program TALOS+ [36].

Table 1
Statistics on data collection and refinement.

	UNE-N (SAD)	UNE-N	CD of NRS
A. Data collection			
Beamline	PLS-5C	PLS-5C	Photon Factory (AR-NW12A)
Space group	$P6_522$	$P6_5$	$P2_12_12_1$
Unit cell lengths (Å)	32.724, 32.724, 218.861	32.626, 32.626, 215.921	113.350, 127.103, 163.475
Unit cell angles (°)	90, 90, 120	90, 90, 120	90, 90, 90
Peak			
X-ray wavelength (Å)	0.9796	0.9999	1.0000
Resolution range (Å)	50.00–1.90 (1.93–1.90)[a]	50.00–1.65 (1.68–1.65)[a]	50.00–2.25 (2.29–2.25)[a]
R_{merge}[b]	0.091 (0.401)[a]	0.102 (0.482)[a]	0.099 (0.467)[a]
$\langle I\rangle/\langle\sigma(I)\rangle$	33.2 (12.5)[a]	15.2 (4.1)[a]	19.8 (4.5)[a]
Completeness (%)	99.7 (100.0)[a]	93.7 (94.3)[a]	100.0 (100.0)[a]
Redundancy	35.5 (38.1)[a]	7.1 (6.3)[a]	7.3 (7.1)[a]
B. Model refinement			
PDB code		4ZYA	5XIX
Resolution (Å)		30.00–1.65	30.00–2.25
No. reflections		14,572	112,318
R_{work}/R_{free}[c] (%)		20.8/26.0	18.0/23.1
No. of non hydrogen atoms/average B-factor (Å^2)			
Protein		1184/24.26	13,690/34.68
Ligand/ion		9/28.10	162/38.74
Water		135/26.73	1106/36.85
R.m.s. deviations from ideal geometry			
Bond lengths (Å)		0.010	0.008
Bond angles (°)		1.130	1.101
Ramachandran[d]			
Favored/outliers (%)		98.6/0.0	97.0/0.4
Poor rotamers (%)		0.8	0.8

[a] Values in parentheses refer to the highest resolution shell.
[b] $R_{merge} = \Sigma_h\Sigma_i|I(h)_i - \langle I(h)\rangle| / \Sigma_h\Sigma_i I(h)_i$, where $I(h)$ is the intensity of reflection h, Σ_h is the sum over all reflections, and Σ_i is the sum over i measurements of reflection h.
[c] $R_{work} = \Sigma||F_{obs}| - |F_{calc}|| / \Sigma|F_{obs}|$, where R_{free} is calculated for a randomly chosen 5% of reflections, which were not used for structure refinement and R_{work} is calculated for the remaining reflections.
[d] Values obtained using *MolProbity*.

2.5. Cell culture and materials

A549, H460, WI-26, Daudi, Jurkat, and J774A.1 cells were grown in RPMI1640 medium (Hyclone, Logan, UT, USA) containing 10% fetal bovine serum and antibiotics (100 UI penicillin and 100 μg/mL streptomycin). DMEM medium containing the same supplements was used for RAW 264.7 culture. Antibodies against NRS, tubulin, and CCR3 were purchased from Abcam (Cambridge, UK), Sigma-Aldrich, and Millipore (Billerica, MA, USA), respectively.

2.6. Cell migration assay

Cell migration was determined by using a Transwell plate (5 μm pore size, 24-well, Corning). Cells were seeded in the upper chamber which had been pre-coated with 20 μg/mL fibronectin (BD Biosciences, Franklin Lakes, NJ, USA). NRS, UNE-N, and CD were separately added to the lower chamber as attractants and CCL5 as a positive control. After 4 h incubation, cells embedded in the fibronectin coated-membrane were fixed and stained with hematoxylin (Sigma-Aldrich). Non-migrated cells were removed with a cotton swab. The membrane was excised and mounted on slide glass. Migrated cells were monitored by microscopy using a 20× objective lens.

2.7. Secretion assay

Cells were seeded and then cultured to 70% confluency. Cells were washed twice with PBS and then incubated under different conditions. Cultured media were harvested and then sequentially centrifuged at 1000 ×*g* for 10 min and 10,000 × *g* for 20 min to remove cells and debris, respectively. To precipitate proteins, TCA (Sigma-Aldrich) was added to a 10% final concentration. After 12 h incubation, secreted proteins were pelleted by 20,000 ×*g* centrifugation. Precipitated proteins were resuspended in 100 mM HEPES (pH 8.0) and then separated by SDS-PAGE for immunoblotting.

2.8. Immunoblotting

Cells were lysed on ice by M-PER mammalian protein extraction reagent (Pierce Biotechnology, Waltham, MA, USA). After removing cell debris by centrifugation, protein concentration was measured using Bradford solution (Bio-Rad, Hercules, CA, USA). Proteins were separated by SDS-PAGE and then transferred to polyvinylidene fluoride membrane for immunoblotting with specific antibodies.

2.9. Pull-down assay

Four MBP-fused CCR3 EDs were incubated with NRS, UNE-N, CD, or CCL5 in PBS containing 5% glycerol, respectively. After 2 h incubation, amylose-resin (New England Biolabs, Ipswich, MA, USA) was added to pull down MBP-fused proteins. Precipitated proteins were resolved and separated by SDS-PAGE. Co-precipitated proteins with MBP-fused CCR3 EDs were detected by Coomassie blue staining (Expedeon, San Diego, CA, USA).

2.10. Statistical analysis

Statistical analysis was performed using Dunnett's multiple comparison test and two-tailed Student's *t*-test. All graphs are presented as the mean ± standard deviation (SD). Differences were considered statistically significant at a P value < 0.05.

2.11. Data deposition

The coordinates and structure factors of UNE-N and CD of human NRS have been deposited in the Protein Data Bank (http://www.rcsb.org) under ID codes 4ZYA and 5XIX, respectively.

3. Results

3.1. UNE-N shares a structural scaffold with the chemotactic N-terminal domain of BmNRS but exhibits unique features

Human NRS is composed of UNE-N, an anticodon-binding domain (ABD), a hinge region (HR), and a catalytic domain. We determined the crystal structures of UNE-N (residues 4–77) and CD (residues 98–548) of NRS at 1.65 and 2.25 Å, respectively (Fig. 1A). UNE-N is composed of two α-helices (α1, α2) and three β-strands (β1, β2, β3) with β1-α1-β2-β3-α2 topology. Three β-strands form a parallel/antiparallel mixed β-sheet (Fig. 1B). DALI server analysis for structural similarity searching with known protein structures [37] predicted that the most similar structure to UNE-N is the UNE-N domain from *B. malayi* (PDB ID: 2KQR) with a *Z*-score of 7.3 and 27% amino acid sequence identity. Despite the low sequence identity, superposition of the UNE-N structures of human NRS and *B. malayi* NRS (*Bm*NRS) showed that the overall fold is very similar with a root-mean-square deviation (RMSD) of 2.3 Å for all C_α atoms (Fig. 1C). The overall structural similarity of UNE-Ns from human and *B. malayi* initially indicated that the human UNE-N domain also plays a chemokine-like role similarly to UNE-N of *B. malayi*. The lysine-rich helical motif, i**SK**sq**LK**nik**K,** was also observed at the N-

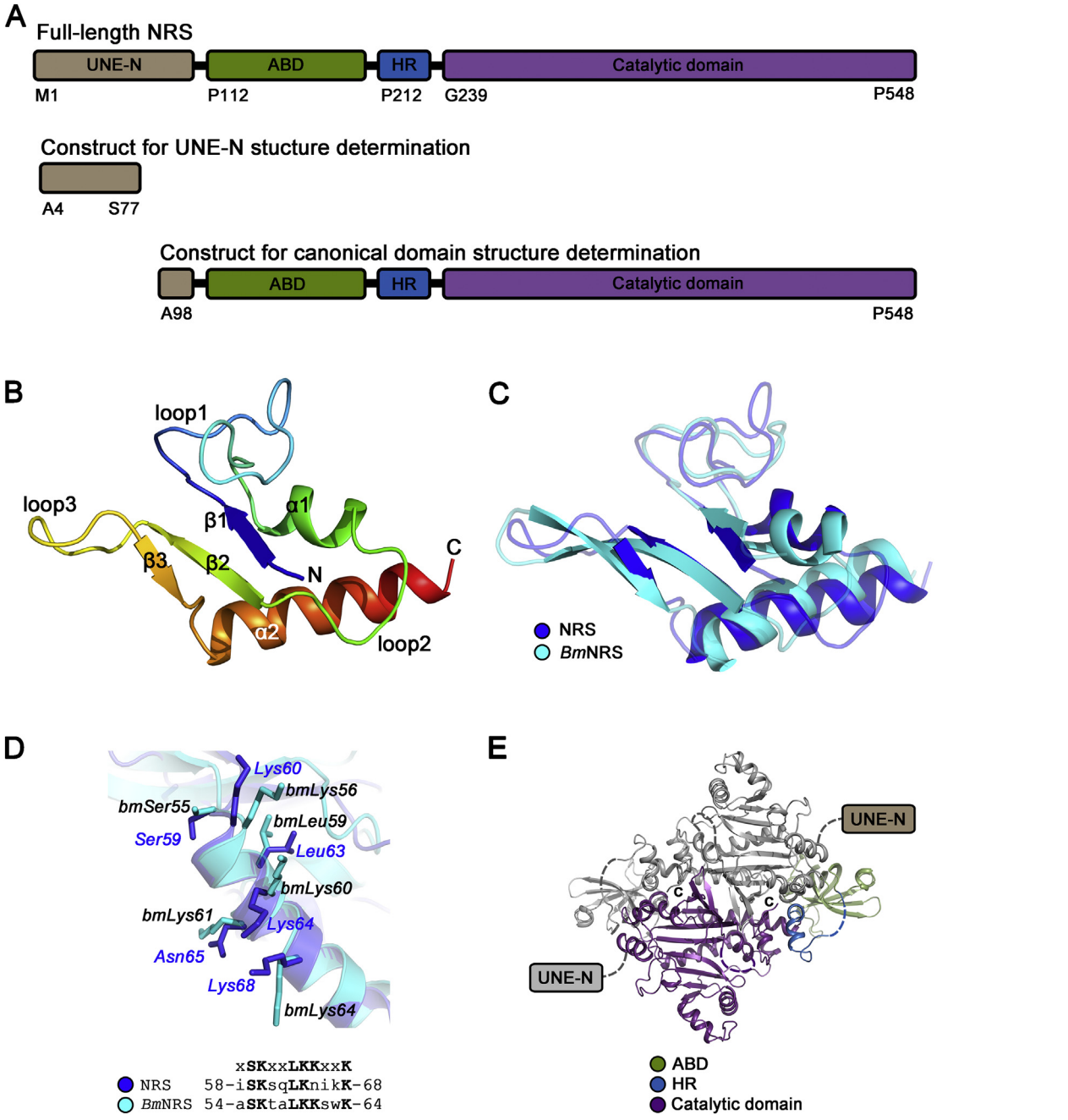

Fig. 1. Overall structure of NRS. (A) Domain composition of NRS. UNE-N, ABD, and HR indicate N-terminal extension domain, anticodon-binding domain, and hinge region, respectively. Three NRS constructs with full-length (residue 1–548), UNE-N (residue 4–77), and canonical domain (CD, residue 98–548) were used for structure determination and biological experiments. (B) Crystal structure of UNE-N. Rainbow cartoon representation of UNE-N depicts amino acid residues from N-terminus to C-terminus in blue to red, respectively. (C) Secondary structure match (SSM) superposition of UNE-N of NRS with UNE-N of *Bm*NRS (PDB ID: 2KQR). UNE-Ns of NRS and *Bm*NRS are displayed as cartoon representations colored in blue and cyan, respectively. (D) Lysine-rich motifs of UNE-N of NRS and *Bm*NRS are superposed with respect to the main chain of helix α2. Amino acid sequences of each lysine-rich motif are shown below. (E) Crystal structure of CD of NRS. ABD, HR, and catalytic domain are colored in green, blue, and purple, respectively. CD from the homodimeric pair is colored in grey.

terminus of helix α2, which implies its interaction with the substrate tRNA as shown in UNE-N of *B. malayi* [18] (Fig. 1D).

Interestingly, the β2-loop3-β3 region exhibits remarkable structural differences. UNE-N has a longer loop3 with Ser48-Arg54 residues and shorter β-strands in both ends of loop3 (β2 and β3), while UNE-N of *B. malayi* contains a β-hairpin structure with a type II β-turn (Lys5-Asp46-Gly47-Lys48) and longer β-strands. NMR studies of UNE-N showed consistent results for the secondary structure propensity of loop3 in the crystal structure (Supplementary Table 1). In UNE-N of *B. malayi*, the β-hairpin structure that is equivalent to loop3 of human UNE-N may be a minimal motif for the interaction with CXCR1/2 [23]. Based on our structural analysis, loop3 of UNE-N may be the most important region for the interaction with CCR3, and thus for subsequent CCR3-mediated signal transduction, which is further discussed below. In addition, the loop3 region was the most dynamic part in UNE-N from the ^{1}H-^{15}N hetero-nuclear nuclear Overhauser effect (NOE) experiment and the amide proton exchange rate for the loop3 region and N-terminal region of helix α2 were higher than those in the other parts of the protein, further supporting the dynamic nature of the loop3 region (Fig. 2).

We also determined the crystal structure of CD of NRS using the molecular replacement method with the CD of *Bm*NRS as a phasing model. The CD of NRS shares considerable structural similarities with NRSs from *B. malayi*, *Pyrococcus horikoshii*, and *Entamoeba histolytica*, as calculated using the DALI server [37]. The catalytic domain of the CD features a nucleotide-binding site with an antiparallel β-sheet flanked with α-helices, which are structural characteristics of the class 2 ARS family (Fig. 1E). The dimeric interface of CD is widely spread through ABD and the catalytic domain of 3800 Å^2, which covers approximately 18% of the monomeric surface area of CD, as calculated using the PISA (Protein interfaces, surfaces, and assemblies) server [38].

3.2. UNE-N exclusively elicits chemotactic activities of NRS on Daudi and Jurkat cells

To narrow down the functional determinants of NRS for the chemokine activities on lymphocytes, iDCs, and CCR3-transfected HEK-293 cells in a CCR3-dependent manner [4,22] and to examine whether the evolutionarily acquired UNE-N plays a role in the chemokine activity of NRS, we conducted cell migration assays with three different constructs, NRS, UNE-N (residues 1–77), and CD (residues 98–548). Daudi, Jurkat, and H460 cell lines were used as representative B cells, T cells, and cancer cells, respectively, and seeded into the upper chamber coated with fibronectin. Then, the lower chamber media were treated with NRS, UNE-N, and CD at 0.1, 1, and 10 nM. Microscopic analysis showed that NRS and UNE-N induced the migration of Daudi and Jurkat cells, while CD did not affect the migration of any cells. No migration effect was observed for H460 cells, further supporting that the chemokine activity of NRS specifically targets immune cells (Fig. 3A–C). And we added NRS to both the upper chamber and the lower chamber

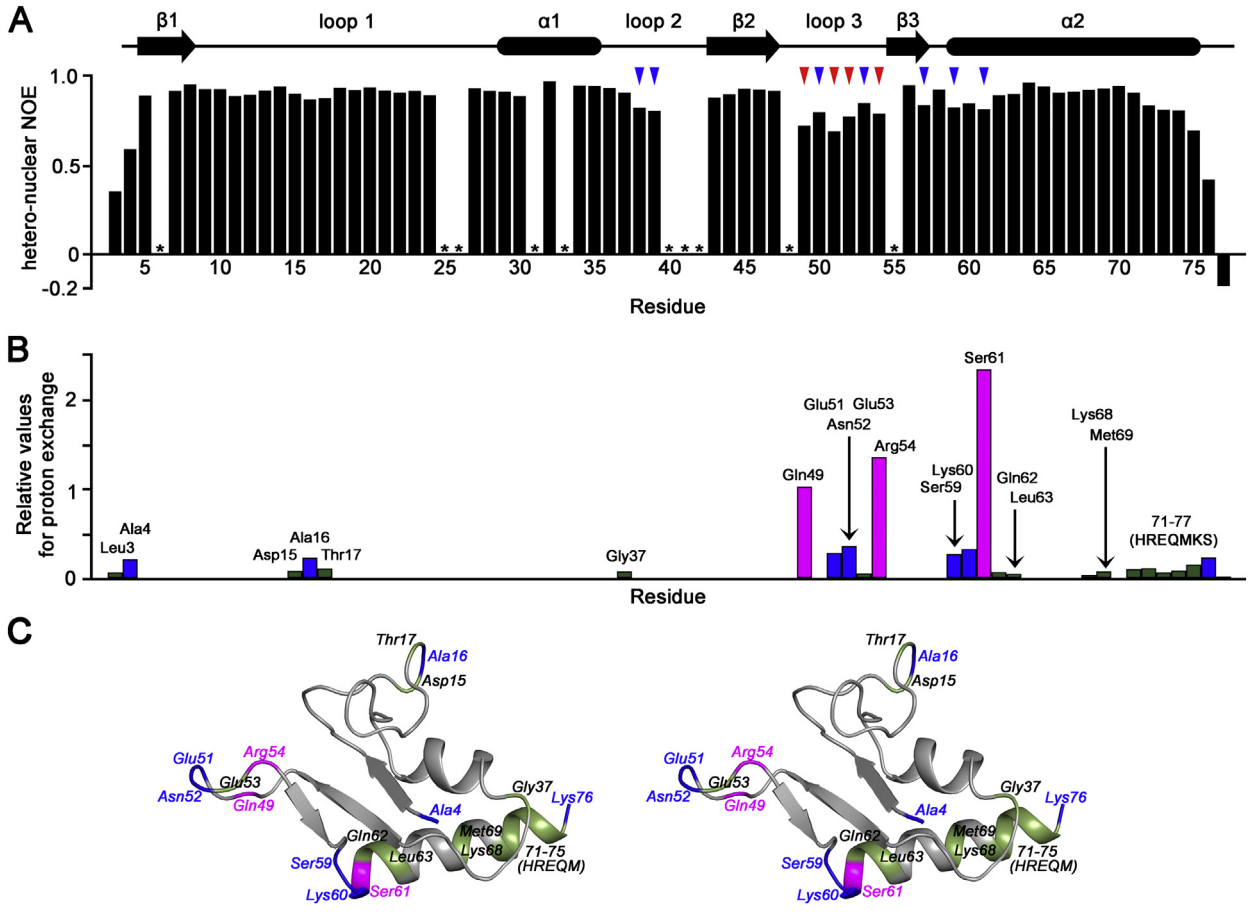

Fig. 2. Dynamics of UNE-N. (A) Hetero-nuclear ^{1}H-^{15}N NOE data of UNE-N. Hetero-nuclear NOE values are plotted against UNE-N residues. Residues showing the lowest and second-lowest NOE values are indicated by red and blue down arrows, respectively (red arrows: hetero-nuclear NOE value < 0.8, blue arrows: 0.8 < hetero-nuclear NOE value < 0.85). N-terminal and C-terminal residues are excluded for potential fast motions. The spectra were recorded at 298 K in buffer containing 150 mM NaCl, 20 mM NaH_2PO_4/Na_2HPO_4 (pH 6.5), and 10% D_2O. The residues showing unclear peaks because of overlaps or inadequate signal to noise (S/N) were omitted and are denoted by * marks. (B) Plot of peak intensities on the CLEANEX-PM spectrum with respect to UNE-N residues. Residues with relative values for proton exchange higher than 1, between 0.1 and 1, and lower than 0.1 are colored in magenta, blue, and green, respectively. The spectrum was obtained with a proton-exchange mixing time of 20 ms and recorded at 298 K in buffer containing 150 mM NaCl, 20 mM NaH_2PO_4/Na_2HPO_4 (pH 6.5), and 10% D_2O. (C) Stereo-view image of UNE-N on which residues are mapped and colored as in (B).

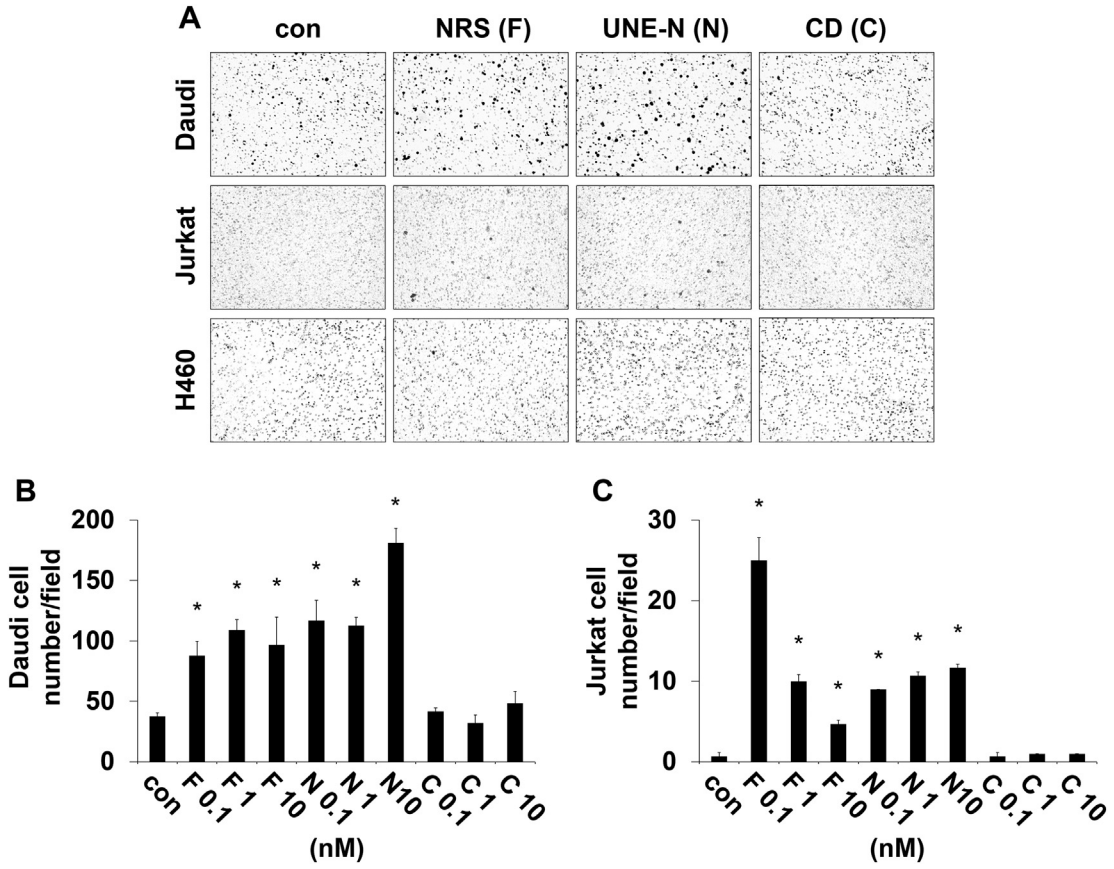

Fig. 3. Chemokine activity of UNE-N. (A) Cell migration induced by NRS. Daudi, Jurkat, and H460 cells were used as representative B cells, T cells, and cancer cells, respectively. The cells were seeded in the fibronectin-coated upper chamber of the Transwell. NRS, UNE-N, and CD were added to the lower chamber at 1 nM concentration. After 4 h incubation, fibronectin-coated membranes were harvested. Migrated cells embedded in the harvested membrane were stained and then monitored by microscopy. (B,C) Cell migrations induced by different concentrations of NRS. Migration of Daudi (B) and Jurkat (C) cells was quantified by cell counting. Labels on the X-axis represent NRS construct and concentration: F, full-length NRS; N, UNE-N; C, CD. Error bars indicate the mean ± standard deviation from the average of three independent experiments. Significant differences were determined by Dunnett's multiple comparison test. $^{*}P < 0.05$.

and observed that the migration of Jurkat cells was blocked, which implies that NRS induced chemotaxis rather than chemokinesis (Supplementary Fig. 3). Collectively, our data reveal that the evolutionally acquired UNE-N is a functional motif necessary and sufficient for inducing migration of Daudi and Jurkat cells.

3.3. UNE-N directly interacts with CCR3 extracellular domains

To further elucidate whether UNE-N exerts its chemokine activity via CCR3, we evaluated the CCR3 expression levels in H460, Daudi, and Jurkat cells (Fig. 4A). We examined the migration of Daudi and Jurkat cells by UNE-N when CCR3 expression was suppressed by a specific CCR3-targeting siRNA (si-CCR3). The chemokine activities of NRS and UNE-N were significantly reduced as CCL5, a well-established chemokine of CCR3 [39], which was used as a positive control (Fig. 4D,E). These results indicate that UNE-N elicits chemokine activity via CCR3 as a possible functional receptor.

We next evaluated the in vitro interaction between NRS and CCR3 EDs to narrow down the binding propensities of UNE-N with respect to CCR3 EDs. CCR3 ED1, ED2, ED3, and ED4 with a maltose-binding protein (MBP) tag at each N-terminus were purified and incubated with NRS, UNE-N, CD, or CCL5. MBP control without CCR3 EDs did not pull down NRS, UNE-N, CD, and CCL5. Interestingly, NRS and UNE-N were co-precipitated with CCR3 EDs, while CD and CCL5 were not pulled down (Fig. 4F–I). Particularly, CCR3 ED3 bound more strongly to NRS/UNE-N than CCR3 ED1 or ED2 did and we observed weak interaction between CCR3 ED4 and NRS/UNE-N. CCL5 was not co-precipitated with CCR3 EDs, which needs further attention regarding to the condition of in vitro interaction between CCL5 and CCR3 EDs as will be discussed below. Our results indicate that UNE-N exerts CCR3-mediated chemokine activity and directly interacts with CCR3 ED3, ED2/ED1, and ED4, listed in the order of affinity.

3.4. Loop3 of UNE-N is an effector motif for CCR3 interactions

To further investigate the binding mode of UNE-N to CCR3, we compared the ^{1}H-^{15}N HSQC spectra of UNE-N in the absence and presence of four individual CCR3 EDs. We observed that CCR3 ED3 caused the most perturbed spectra peaks with predominant resonance broadenings rather than chemical shift perturbations. Overall resonance broadenings can be explained by the remarkable increases in transverse relaxation rates (R2) of UNE-N when it bound to MBP-fused CCR3 EDs. Similar peak changes were observed in the spectra of UNE-N titrated with CCR3 ED1 to a lesser extent. CCR3 ED2 caused slight resonance broadening without chemical shift changes and CCR3 ED4 did not cause noticeable spectral changes. These results indicate that the binding preference for UNE-N is CCR3 ED3, ED1, ED2, and ED4, in descending order, which is consistent with our pull-down assay results in that UNE-N binds most strongly to CCR3 ED3.

The degrees of resonance broadenings may be derived from the ratios of peak intensities of the spectra in the absence and presence of CCR3 EDs. When these values elicited by CCR3 ED3, ED1, and ED2 were plotted with respect to UNE-N residues, the average ratio/standard deviation for each plot was 0.530/0.066 (ED3), 0.575/0.052 (ED1), and 0.794/0.056 (ED2), respectively (Fig. 5). Larger standard deviation values for UNE-N residues can be interpreted as more specific

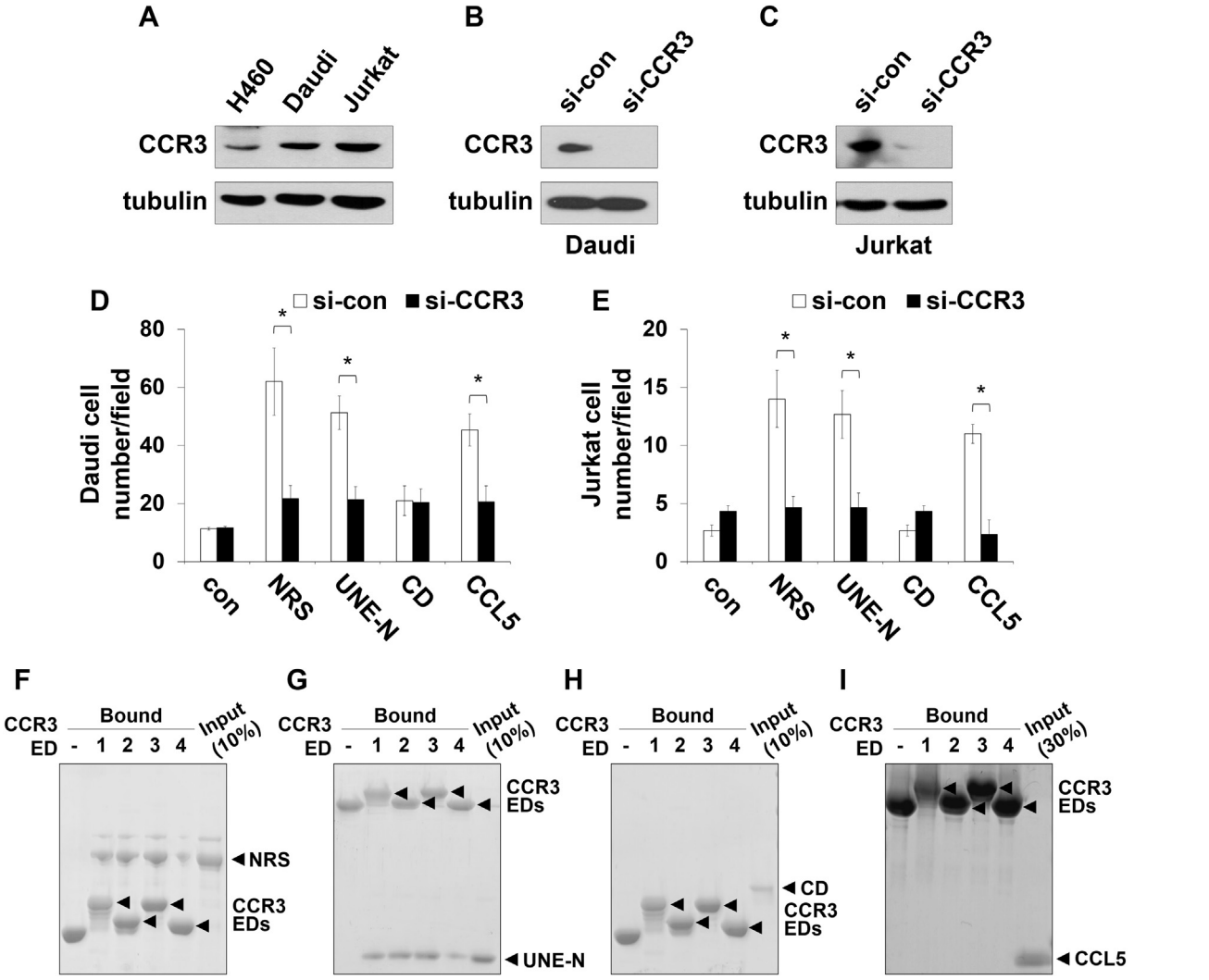

Fig. 4. Direct interaction of UNE-N with CCR3. (A) CCR3 expression in H460, Daudi, and Jurkat cells was determined by immunoblotting. (B,C) Confirmation of CCR3 knock-down by si-CCR3. CCR3 expression in Daudi (B) and Jurkat (C) cells after si-CCR3 treatment was determined by immunoblotting. (D,E) Effect of CCR3 knock-down on NRS-induced cell migration of Daudi (D) and Jurkat (E) cells. The cells down-regulated by CCR3-targeting siRNA (si-CCR3) were used for the Transwell migration assay. After NRS, UNE-N, and CD at 1 nM concentration were added to the lower chamber, while migrated cells were counted in the membrane of the upper chamber. CCL5, a well-known chemokine of CCR3, was used as the positive control. Error bars indicate the mean ± standard deviation from the average of three independent experiments. Significant differences were determined by Student's *t*-test. *$P < 0.05$. (F-I) Interaction between NRS and CCR3 EDs. For in vitro binding assay, MBP control without CCR3 EDs (lane '-') and four MBP-fused CCR3 EDs (ED1–ED4, lanes 1–4) were separately incubated with NRS (F), UNE-N (G), CD (H), and CCL5 (I), and then precipitated by maltose resin. Co-precipitated proteins were resolved by SDS-PAGE and detected by Coomassie blue staining.

interactions of UNE-N with CCR3 EDs. UNE-N residues are specifically affected by CCR3 binding, and residue-by-residue analysis of UNE-N would reveal the binding mode more in detail.

To identify the interacting residues of UNE-N with each CCR3 ED, we quantified the resonance broadenings and chemical shift perturbations. In the presence of CCR3 ED3, Glu51 and Asn52 in loop3 and Lys60 in helix α2 showed the largest resonance broadenings (Fig. 5A). Considering that the conformational change on the intermediate NMR time scale increases resonance broadening of corresponding peaks, loop3 with Glu51 and Asn52 undergo the most remarkable conformational change and Lys60 at the N-terminus of helix α2 is affected when UNE-N interacts with CCR3 ED3. Slight chemical shift perturbations upon binding to CCR3 ED3 were observed for Ala4, Tyr7, Ala16, Lys50, Ile58, Gln62, Ile66, His71, Gln74, Met75, Lys76, and Ser77 (Supplementary Fig. 4), suggesting slight structural changes on the fast NMR time scale.

Following titration with CCR3 ED1, Gln49 in loop3 showed the largest resonance broadening, while Glu51, Asn52, and Lys60 showed the second largest broadening (Fig. 5B), supporting that loop3 of UNE-N is mainly involved in binding to CCR3 ED1. Chemical shift perturbations upon binding to CCR3 ED1 were observed for Ala4, Ala16, Lys50, Ile58, Met75, Lys76, and Ser77, with lower values than those caused by CCR3 ED3 (Supplementary Fig. 5). Similar to the titration with CCR3 ED1, Gln49 in loop3 elicited the largest resonance broadening and Glu51, Asn52, Arg54, and Lys60 caused the second largest in the presence of CCR3 ED2 (Fig. 5C). Collectively, these results suggest that loop3 in UNE-N plays a major role in binding to CCR3 and is an effector motif for receptor recognition.

3.5. Loop3 region of UNE-N is structurally distinct from UNE-N of BmNRS targeting different receptors

To gain insights into the structural contribution of loop3 of UNE-N in target receptor selection, we aligned nine UNE-N sequences from representative eukaryotes; human, monkey, mouse, bird, frog, fish, insect, and two nematodes (Fig. 6A). We found that two aromatic amino acid residues near loop3, Tyr7 and Trp55, are highly conserved among various NRSs. Comparison of the structures of UNE-N from human and *B. malayi* revealed that the secondary structure composition of loop3

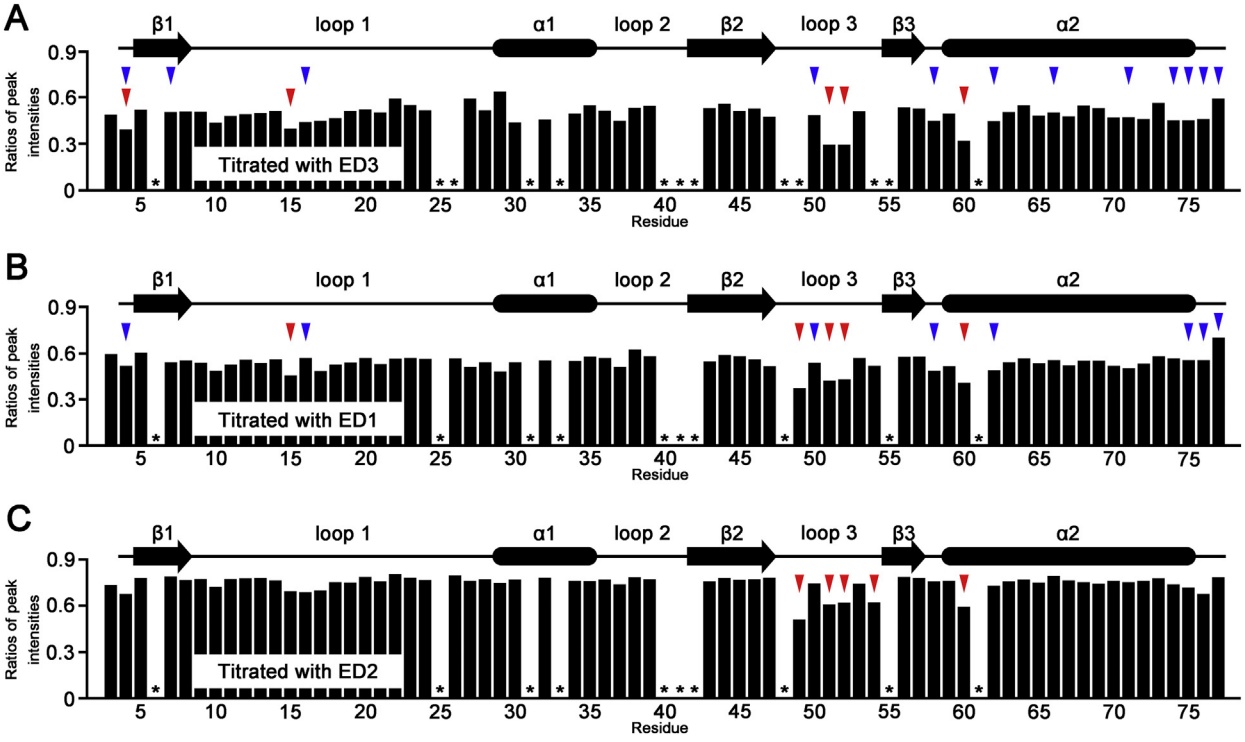

Fig. 5. Key residues of UNE-N involved in the interaction with CCR3. (A–C) Ratios of peak intensities are plotted against UNE-N residues in the presence of CCR3 ED3 (A), ED1 (B), and ED2 (C), each of which is fused to MBP. The molar ratio of UNE-N of NRS to MBP-fused CCR3 EDs used was approximately 1:1. Residues showing large resonance broadening (ratio < 0.85) and chemical shift perturbations are marked with red and blue down arrows, respectively. All titration experiments were carried out at 298 K in buffer containing 150 mM NaCl, 20 mM NaH_2PO_4/Na_2HPO_4 (pH 7.5), and 10% D_2O. Residues showing unclear peaks because of overlaps or inadequate signal to noise (S/N) were omitted and are denoted by * marks.

region was notably different, although the overall structures were very similar and some characteristic residues near loop3 region are highly conserved.

The aromatic side chains of Tyr7 and Trp55 of NRS interact with each other via a pi-pi interaction, stabilizing protein folding. On the opposite side of the Typ7-Trp55 interface, the side chain of Arg54, which is conserved in vertebrates, also stabilized Trp55 via a cation-pi interaction according to *CaPTURE* web server calculations [40]. Additionally, the negatively charged carboxyl group of Asp47, which is conserved in vertebrates, stabilized the positively charged guanidinium group of Arg54 electrostatically. For UNE-N of *Bm*NRS, Tyr4 and Trp51 correspond to Tyr7 and Trp55 of NRS, respectively, and form a pi-pi interaction through aromatic side chains of Tyr-Trp. However, *Bm*NRS lacks the basic residue corresponding to Arg54 of NRS, but the positively charged guanidinium group of Arg42 (equivalent to Asp47 of NRS) alternatively occupies the Arg54 site of NRS and interacts with Trp51 via a cation-pi interaction (Fig. 6B). The stable conformation of Arg54 of NRS induces forced bending of the peptide backbone of Glu53-Arg54-Trp55 and the region forms a loop, while *Bm*NRS adopts an antiparallel β-sheet structure in the region. Together with our NMR titration results, the different conformation of the loop3 region may explain the target receptor specificity of UNE-Ns.

4. Discussion

Evolutionary pressure to obtain novel functions in eukaryotic cell systems has resulted in the incorporation of non-translational additional domains into ARSs and has maintained ARS splicing variants with catalytic nulls [10,41]. In NRS, domain addition at the N-terminus (UNE-N) has been observed, but specific functional roles elicited by UNE-N remain unclear. Our crystal structure of UNE-N of NRS provides functional insight, as the overall structure was similar to the chemotactic UNE-N domain of *Bm*NRS which interacts with two chemokine receptors, CXCR1 and CXCR2.

The UNE-N domains of human NRS and *Bm*NRS are structurally similar and both exhibit non-translational chemokine activities that induce the migration of immune cells. Interestingly, structurally similar UNE-Ns from human NRS and *Bm*NRS target different chemokine receptors, CCR3 and CXCR1/2, respectively, and it is very important to elucidate how these structurally similar domains can recognize their matching receptors. To investigate how this novel domain fold interacts with chemokine receptors and why each UNE-N targets different receptors, we elucidated the interaction mode between UNE-N of NRS and CCR3 EDs by conducting pull-down assays and NMR perturbation experiments. Our pull-down assay results may not demonstrate a physical interaction between UNE-N and 'native' CCR3 but clearly shows that UNE-N interacts with EDs derived from CCR3. If UNE-N did not interact with CCR3 at all, UNE-N would not be pulled down together with CCR3 EDs in the in vitro pull-down assay [42]. CCL5, a CCR3-targeting chemokine, was not pulled down together with MBP-fused CCR3 EDs. When CCL5 binds to chemokine receptors, post-translational modification such as tyrosine sulfation could be a key factor [43]. Thus, we might not observe the interaction between CCL5 and MBP-fused CCR3 EDs in our pull-down assay experiments since MBP-fused CCR3 EDs were purified from *E. coli* and would not contain necessary post-translational modifications for the interaction.

In addition to the in vitro pull-down assay, we implemented NMR perturbation experiments with UNE-N and CCR3 EDs which further support the direct interaction between UNE-N and CCR3 EDs. NMR perturbation experiment was also used for the validation of interactions between CCR3 and CCL11 (eotaxin-1), a well-known CCR3 chemokine, in which a synthesized ED1 peptide derived from CCR3 was used [44]. Additionally, the interaction between CCL5 and CCR5 was investigated in a similar way to our NMR spectrometry experiments, using peptides derived from CCR5 EDs [45]. Taken all together, our data from pull-down

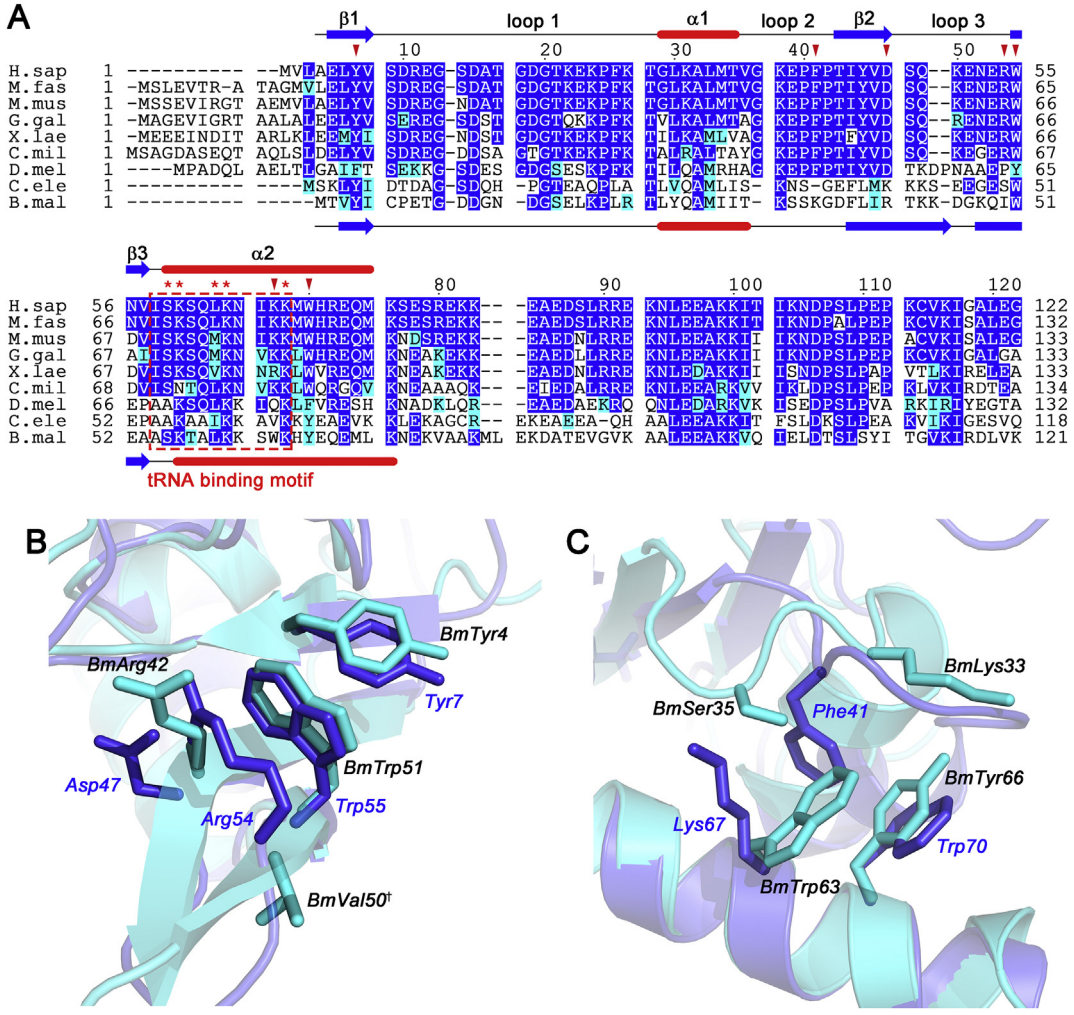

Fig. 6. Structural analysis of UNE-N for receptor specificity. (A) Sequence alignment of UNE-N regions from nine eukaryotic NRSs: H.sap, *Homo sapiens*; M.fas, *Macaca fascicularis*; M.mus, *Mus musculus*; G.gal, *Gallus gallus*; X.lae, *Xenopus laevis*; C.mil, *Callorhinchus milii*; D.mel, *Drosophila melanogaster*; C.ele, *Caenorhabditis elegans*; B.mal, *Brugia malayi*. Residues same or conserved in UNE-Ns are colored in blue or cyan, respectively. Secondary structure elements of NRS and *Bm*NRS are represented above and below the sequences with red tube for α-helix and blue arrow for β-strand, respectively. Representative residues of conformational importance are denoted with red down arrows. tRNA binding motif is marked with *. (B) Residues on β2-loop3-β3 region of UNE-N of human NRS and *Bm*NRS. C_α atoms of Trp55-Ser59 of human NRS and Trp51-Ser55 of *Bm*NRS are superposed. Human NRS and *Bm*NRS are colored in blue and cyan, respectively (*BmVal50*†, Leu50 of *Bm*NRS is replaced with valine in NMR structure of UNE-N of *Bm*NRS). (C) Residues on loop2 and helix α2 region of UNE-N from NRS and *Bm*NRS. NRS and *Bm*NRS structures are represented as in (B).

experiments and NMR perturbation experiments would provide reliable evidences for the direct interaction between UNE-N and CCR3.

NMR perturbation experiment is a powerful tool as well for probing the interfaces of a protein with its binding partner [46,47]. According to the perturbation experiment for ^{15}N-labeled UNE-N with MBP-fused CCR3 EDs, we detected peaks showing more sensitive broadening than those of other peaks, which is often observed following titration with a protein ligand. However, the degree of chemical shift was not sufficient to assign specific residues affected by the titration experiments (Supplementary Figs. 4,5). The degrees of peak broadening of UNE-N residues were affected by addition of CCR3 ED3, ED1, and ED2 in the order of reducing sensitivity while maintaining similar broadening patterns plotted by UNE-N residues. We confirmed that residues in the loop3 region of UNE-N were mainly influenced by titration with CCR3 EDs. For UNE-N of *Bm*NRS, the β2-loop3-β3-α2 motif has been suggested to interact with CXCR1/2 based on structural comparison with other chemokines [23]. The β2-loop3-β3 regions of UNE-N in NRS and *Bm*NRS are quite different in amino acid sequence and structure as described above. Thus, different conformations in the determinant β2-loop3-β3 region of UNE-Ns may mainly contribute to the selection of their target receptors. Additionally, we found that Trp70 in human NRS, equivalent to Tyr66 in *Bm*NRS, is a highly conserved aromatic residue in helix α2 and forms a pi-pi interaction with Phe41 in the adjacent loop2, while Tyr66 in *Bm*NRS forms a pi-pi interaction with Trp63 in the same α2 helix (Fig. 6C). This subtle structural difference may leave loop2 of *Bm*NRS more flexible than that of human NRS, conferring an assistant role in recognizing target receptors.

As shown in the cell migration assay with UNE-N and other constructs of NRS, UNE-N exhibited chemokine activity in CCR3-expressing cells. Considering that autoantibodies against NRS have been detected in the sera of autoimmune patients [48,49], the chemokine activity of NRS could be closely related to proinflammatory signaling. Although NRS is a cytosolic protein, its autoantibodies, anti-KS, has been detected in the sera of patients with autoimmune diseases such as ILD and myositis [48–52]. ILD is a well-known major clinical feature of patients with anti-KS and secreted NRS may elicit CCR3-mediated proinflammatory signaling in ILD development. Thus, modulators of the NRS-CCR3 signaling axis may provide a niche for elucidating the mechanism of ILD and alleviating CCR3-mediated malignances. The immunogenicity of antigenic materials interacting with receptors on antigen-presenting cells is highly augmented and the balance among immunomodulatory cytokines is a key factor in the life and death of cells [53,54].

In the pull-down assay and NMR perturbation experiments, we suggest that subtle conformational differences between UNE-Ns of human NRS and *Bm*NRS discern the target receptor. Loop3 in UNE-N of NRS is a key region for the interaction with ED3, ED1, and ED2 of CCR3 in the order of descending affinity. Cytosolic NRS secretion from cells and specific targeting of CCR3 on immune cells may be explained as a "danger signal" from cells confronting stressful environments [4,55]. However, the exact roles of autoantibodies against secreted NRS and pathophysiological connections between NRS-CCR3 signaling and immune diseases require further investigations. Structural information of UNE-N and CD of NRS at an atomic level and the interaction mode between UNE-N and CCR3 may provide a foundation for evaluating NRS-CCR3 signaling and its correlation with autoimmune diseases, in which development of anti-KS has been observed.

Conflict of interest

The authors declare no conflict of interest.

Acknowledgements

We thank the staff members of the beamlines, PLS-5C of Pohang Accelerator Laboratory (Pohang, Republic of Korea) and AR-NW12A of the Photon Factory (Tsukuba, Japan), for X-ray crystallography.

Funding

This work was supported by the Global Frontier Project (grants number: NRF-2013M-3A6A-4043695) and Tumor Microenvironment Global Core Research Center (grant number: 2011-0030001) funded through the National Research Foundation from the Ministry of Science and ICT of Korea.

Appendix A. Supplementary data

Supplementary data to this article can be found online at https://doi.org/10.1016/j.ijbiomac.2018.08.171.

References

[1] C. Manole, C. Inimioara Mihaela, C. Bogdan, New insights into antisynthetase syndrome, Maedica 11 (2) (2016) 130–135.
[2] M. Mahler, F.W. Miller, M.J. Fritzler, Idiopathic inflammatory myopathies and the anti-synthetase syndrome: a comprehensive review, Autoimmun. Rev. 13 (4–5) (2014) 367–371.
[3] Y. Hamaguchi, M. Fujimoto, T. Matsushita, K. Kaji, K. Komura, M. Hasegawa, M. Kodera, E. Muroi, K. Fujikawa, M. Seishima, H. Yamada, R. Yamada, S. Sato, K. Takehara, M. Kuwana, Common and distinct clinical features in adult patients with anti-aminoacyl-tRNA synthetase antibodies: heterogeneity within the syndrome, PLoS One 8 (4) (2013), e60442.
[4] O.M.Z. Howard, H.F. Dong, D. Yang, N. Raben, K. Nagaraju, A. Rosen, L. Casciola-Rosen, M. Hartlein, M. Kron, D. Yang, K. Yiadom, S. Dwivedi, P.H. Plotz, J.J. Oppenheim, Histidyl-tRNA synthetase and asparaginyl-tRNA synthetase, autoantigens in myositis, activate chemokine receptors on T lymphocytes and immature dendritic cells, J. Exp. Med. 196 (6) (2002) 781–791.
[5] P.H. Plotz, The autoantibody repertoire: searching for order, Nat. Rev. Immunol. 3 (1) (2003) 73–78.
[6] M.C. Park, T. Kang, D. Jin, J.M. Han, S.B. Kim, Y.J. Park, K. Cho, Y.W. Park, M. Guo, W. He, X.L. Yang, P. Schimmel, S. Kim, Secreted human glycyl-tRNA synthetase implicated in defense against ERK-activated tumorigenesis, Proc. Natl. Acad. Sci. U. S. A. 109 (11) (2012) E640–E647.
[7] S.W. Lee, B.H. Cho, S.G. Park, S. Kim, Aminoacyl-tRNA synthetase complexes: beyond translation, J. Cell Sci. 117 (Pt 17) (2004) 3725–3734.
[8] M. Guo, P. Schimmel, X.L. Yang, Functional expansion of human tRNA synthetases achieved by structural inventions, FEBS Lett. 584 (2) (2010) 434–442.
[9] S. Kim, S. You, D. Hwang, Aminoacyl-tRNA synthetases and tumorigenesis: more than housekeeping, Nat. Rev. Cancer 11 (10) (2011) 708–718.
[10] W.S. Lo, E. Gardiner, Z. Xu, C.F. Lau, F. Wang, J.J. Zhou, J.D. Mendlein, L.A. Nangle, K.P. Chiang, X.L. Yang, K.F. Au, W.H. Wong, M. Guo, M. Zhang, P. Schimmel, Human tRNA synthetase catalytic nulls with diverse functions, Science 345 (6194) (2014) 328–332.
[11] S.V. Kyriacou, M.P. Deutscher, An important role for the multienzyme aminoacyl-tRNA synthetase complex in mammalian translation and cell growth, Mol. Cell 29 (4) (2008) 419–427.
[12] P.S. Ray, A. Arif, P.L. Fox, Macromolecular complexes as depots for releasable regulatory proteins, Trends Biochem. Sci. 32 (4) (2007) 158–164.
[13] S. Cusack, M. Hartlein, R. Leberman, Sequence, structural and evolutionary relationships between class 2 aminoacyl-tRNA synthetases, Nucleic Acids Res. 19 (13) (1991) 3489–3498.
[14] V.S. Reed, D.C. Yang, Characterization of a novel N-terminal peptide in human aspartyl-tRNA synthetase. Roles in the transfer of aminoacyl-tRNA from aminoacyl-tRNA synthetase to the elongation factor 1 alpha, J. Biol. Chem. 269 (52) (1994) 32937–32941.
[15] B. Rees, J. Cavarelli, D. Moras, Conformational flexibility of tRNA: structural changes in yeast tRNA(Asp) upon binding to aspartyl-tRNA synthetase, Biochimie 78 (7) (1996) 624–631.
[16] M. Francin, M. Kaminska, P. Kerjan, M. Mirande, The N-terminal domain of mammalian Lysyl-tRNA synthetase is a functional tRNA-binding domain, J. Biol. Chem. 277 (3) (2002) 1762–1769.
[17] H.K. Cheong, J.Y. Park, E.H. Kim, C. Lee, S. Kim, Y. Kim, B.S. Choi, C. Cheong, Structure of the N-terminal extension of human aspartyl-tRNA synthetase: implications for its biological function, Int. J. Biochem. Cell Biol. 35 (11) (2003) 1548–1557.
[18] T. Crepin, F. Peterson, M. Haertlein, D. Jensen, C. Wang, S. Cusack, M. Kron, A hybrid structural model of the complete *Brugia malayi* cytoplasmic asparaginyl-tRNA synthetase, J. Mol. Biol. 405 (4) (2011) 1056–1069.
[19] K.R. Kim, S.H. Park, H.S. Kim, K.H. Rhee, B.G. Kim, D.G. Kim, M.S. Park, H.J. Kim, S. Kim, B.W. Han, Crystal structure of human cytosolic aspartyl-tRNA synthetase, a component of multi-tRNA synthetase complex, Proteins 81 (10) (2013) 1840–1846.
[20] M. Kron, K. Marquard, M. Hartlein, S. Price, R. Leberman, An immunodominant antigen of *Brugia malayi* is an asparaginyl-tRNA synthetase, FEBS Lett. 374 (1) (1995) 122–124.
[21] M. Kron, M. Petridis, Y. Milev, J. Leykam, M. Hartlein, Expression, localization and alternative function of cytoplasmic asparaginyl-tRNA synthetase in *Brugia malayi*, Mol. Biochem. Parasitol. 129 (1) (2003) 33–39.
[22] B.L. Ramirez, O.M. Howard, H.F. Dong, T. Edamatsu, P. Gao, M. Hartlein, M. Kron, *Brugia malayi* asparaginyl-transfer RNA synthetase induces chemotaxis of human leukocytes and activates G-protein-coupled receptors CXCR1 and CXCR2, J. Infect. Dis. 193 (8) (2006) 1164–1171.
[23] M.A. Kron, C. Wang, S. Vodanovic-Jankovic, O.M. Howard, L.A. Kuhn, Interleukin-8-like activity in a filarial asparaginyl-tRNA synthetase, Mol. Biochem. Parasitol. 185 (1) (2012) 66–69.
[24] L. Slabinski, L. Jaroszewski, L. Rychlewski, I.A. Wilson, S.A. Lesley, A. Godzik, XtalPred: a web server for prediction of protein crystallizability, Bioinformatics 23 (24) (2007) 3403–3405.
[25] Z. Otwinowski, W. Minor, Processing of X-ray diffraction data collected in oscillation mode, Methods Enzymol. 276 (1997) 307–326.
[26] P.D. Adams, P.V. Afonine, G. Bunkoczi, V.B. Chen, I.W. Davis, N. Echols, J.J. Headd, L.W. Hung, G.J. Kapral, R.W. Grosse-Kunstleve, A.J. McCoy, N.W. Moriarty, R. Oeffner, R.J. Read, D.C. Richardson, J.S. Richardson, T.C. Terwilliger, P.H. Zwart, PHENIX: a comprehensive python-based system for macromolecular structure solution, Acta Crystallogr. D Biol. Crystallogr. 66 (Pt 2) (2010) 213–221.
[27] T.C. Terwilliger, SOLVE and RESOLVE: automated structure solution and density modification, Methods Enzymol. 374 (2003) 22–37.
[28] A.J. McCoy, R.W. Grosse-Kunstleve, P.D. Adams, M.D. Winn, L.C. Storoni, R.J. Read, Phaser crystallographic software, J. Appl. Crystallogr. 40 (Pt 4) (2007) 658–674.
[29] A. Vagin, A. Teplyakov, Molecular replacement with MOLREP, Acta Crystallogr. D Biol. Crystallogr. 66 (Pt 1) (2010) 22–25.
[30] P. Emsley, B. Lohkamp, W.G. Scott, K. Cowtan, Features and development of coot, Acta Crystallogr. D Biol. Crystallogr. 66 (Pt 4) (2010) 486–501.
[31] P.V. Afonine, R.W. Grosse-Kunstleve, N. Echols, J.J. Headd, N.W. Moriarty, M. Mustyakimov, T.C. Terwilliger, A. Urzhumtsev, P.H. Zwart, P.D. Adams, Towards automated crystallographic structure refinement with phenix refine, Acta Crystallogr. D Biol. Crystallogr. 68 (Pt 4) (2012) 352–367.
[32] V.B. Chen, W.B. Arendall 3rd, J.J. Headd, D.A. Keedy, R.M. Immormino, G.J. Kapral, L.W. Murray, J.S. Richardson, D.C. Richardson, MolProbity: all-atom structure validation for macromolecular crystallography, Acta Crystallogr. D Biol. Crystallogr. 66 (Pt 1) (2010) 12–21.
[33] W. Kabsch, C. Sander, Dictionary of protein secondary structure: pattern recognition of hydrogen-bonded and geometrical features, Biopolymers 22 (12) (1983) 2577–2637.
[34] W.G. Touw, C. Baakman, J. Black, T.A. te Beek, E. Krieger, R.P. Joosten, G. Vriend, A series of PDB-related databanks for everyday needs, Nucleic Acids Res. 43 (Database issue) (2015) D364–D368.
[35] F. Delaglio, S. Grzesiek, G.W. Vuister, G. Zhu, J. Pfeifer, A. Bax, NMRPipe: a multidimensional spectral processing system based on UNIX pipes, J. Biomol. NMR 6 (3) (1995) 277–293.
[36] Y. Shen, F. Delaglio, G. Cornilescu, A. Bax, TALOS+: a hybrid method for predicting protein backbone torsion angles from NMR chemical shifts, J. Biomol. NMR 44 (4) (2009) 213–223.
[37] L. Holm, P. Rosenstrom, Dali server: conservation mapping in 3D, Nucleic Acids Res. 38 (Web Server issue) (2010) W545–W549.
[38] E. Krissinel, K. Henrick, Inference of macromolecular assemblies from crystalline state, J. Mol. Biol. 372 (3) (2007) 774–797.
[39] B.L. Daugherty, S.J. Siciliano, J.A. DeMartino, L. Malkowitz, A. Sirotina, M.S. Springer, Cloning, expression, and characterization of the human eosinophil eotaxin receptor, J. Exp. Med. 183 (5) (1996) 2349–2354.
[40] J.P. Gallivan, D.A. Dougherty, Cation-pi interactions in structural biology, Proc. Natl. Acad. Sci. U. S. A. 96 (17) (1999) 9459–9464.
[41] M. Guo, X.L. Yang, P. Schimmel, New functions of aminoacyl-tRNA synthetases beyond translation, Nat. Rev. Mol. Cell Biol. 11 (9) (2010) 668–674.

[42] A. Louche, S.P. Salcedo, S. Bigot, Protein-protein interactions: pull-down assays, Methods Mol. Biol. 1615 (2017) 247–255.
[43] J.P. Ludeman, M.J. Stone, The structural role of receptor tyrosine sulfation in chemokine recognition, Br. J. Pharmacol. 171 (5) (2014) 1167–1179.
[44] C.J. Millard, J.P. Ludeman, M. Canals, J.L. Bridgford, M.G. Hinds, D.J. Clayton, A. Christopoulos, R.J. Payne, M.J. Stone, Structural basis of receptor sulfotyrosine recognition by a CC chemokine: the N-terminal region of CCR3 bound to CCL11/eotaxin-1, Structure 22 (11) (2014) 1571–1581.
[45] L. Duma, D. Haussinger, M. Rogowski, P. Lusso, S. Grzesiek, Recognition of RANTES by extracellular parts of the CCR5 receptor, J. Mol. Biol. 365 (4) (2007) 1063–1075.
[46] M.S. McAlister, H.R. Mott, P.A. van der Merwe, I.D. Campbell, S.J. Davis, P.C. Driscoll, NMR analysis of interacting soluble forms of the cell-cell recognition molecules CD2 and CD48, Biochemistry 35 (19) (1996) 5982–5991.
[47] E.R. Zuiderweg, Mapping protein-protein interactions in solution by NMR spectroscopy, Biochemistry 41 (1) (2002) 1–7.
[48] M. Hirakata, A. Suwa, S. Nagai, M.A. Kron, E.P. Trieu, T. Mimori, M. Akizuki, I.N. Targoff, Anti-KS: identification of autoantibodies to asparaginyl-transfer RNA synthetase associated with interstitial lung disease, J. Immunol. 162 (4) (1999) 2315–2320.
[49] M. Hirakata, A. Suwa, T. Takada, S. Sato, S. Nagai, E. Genth, Y.W. Song, T. Mimori, I.N. Targoff, Clinical and immunogenetic features of patients with autoantibodies to asparaginyl-transfer RNA synthetase, Arthritis Rheum. 56 (4) (2007) 1295–1303.
[50] I.N. Targoff, Update on myositis-specific and myositis-associated autoantibodies, Curr. Opin. Rheumatol. 12 (6) (2000) 475–481.
[51] G.J. Hengstman, B.G. van Engelen, W.T. Vree Egberts, W.J. van Venrooij, Myositis-specific autoantibodies: overview and recent developments, Curr. Opin. Rheumatol. 13 (6) (2001) 476–482.
[52] F. Schneider, R. Aggarwal, D. Bi, K. Gibson, C. Oddis, S.A. Yousem, The pulmonary histopathology of anti-KS transfer RNA synthetase syndrome, Arch. Pathol. Lab. Med. 139 (1) (2015) 122–125.
[53] F. Henry, O. Boisteau, L. Bretaudeau, B. Lieubeau, K. Meflah, M. Gregoire, Antigen-presenting cells that phagocytose apoptotic tumor-derived cells are potent tumor vaccines, Cancer Res. 59 (14) (1999) 3329–3332.
[54] A. Ronchetti, P. Rovere, G. Iezzi, G. Galati, S. Heltai, M.P. Protti, M.P. Garancini, A.A. Manfredi, C. Rugarli, M. Bellone, Immunogenicity of apoptotic cells in vivo: role of antigen load, antigen-presenting cells, and cytokines, J. Immunol. 163 (1) (1999) 130–136.
[55] S. Gallucci, P. Matzinger, Danger signals: SOS to the immune system, Curr. Opin. Immunol. 13 (1) (2001) 114–119.